



Wetting Behavior of Wear-Resistant WC-Co-Cr Cermet Coatings Produced by HVOF: The Role of Chemical Composition and Surface Roughness

Pavel Komarov¹ · David Jech¹ · Serhii Tkachenko¹ · Karel Slámečka¹ · Karel Dvořák² · Ladislav Čelko¹

Submitted: 13 April 2020 / in revised form: 11 November 2020 / Accepted: 17 November 2020 / Published online: 3 January 2021
© ASM International 2021

Abstract Despite the existence of several methods for production of superhydrophobic coatings from various materials, their application in harsh environments is still a great challenge. In this work, WC-Co-Cr cermet coatings were prepared by means of high velocity oxy-fuel (HVOF) spraying. WC particles dispersed in Co-Cr metallic matrix allowed to form the multi-scale surface roughness and thus to achieve hydrophobicity of the coatings in the as-sprayed state. The additional surface treatment by the silicone oil rendered the coatings superhydrophobic. The WC-Co-Cr coatings were fabricated from three different powder feedstocks: coarse powder with coarse WC particles, coarse powder with ultrafine WC particles, and fine powder with ultrafine WC particles. The investigation of microstructure, phase composition, and surface topography of produced coatings was conducted to study the influence of these factors on the water contact angle and surface free energy, which were obtained by the sessile droplet method. Theoretical models were used to explain the wetting behavior of all the coatings. Finally, preliminary results of the slurry abrasion response test revealed very good robustness of hydrophobicity of the coatings and also

pointed to a need for further research on surface modifications for sacrificial applications.

Keywords HVOF · hydrophobic coating · Owens–Wendt theory · slurry abrasion response test · superhydrophobic coating · surface free energy · WC-Co-Cr coating

Introduction

The water wetting behavior of solid surfaces is commonly described by the value of the water contact angle (WCA), which allows to divide all the surfaces into several classes, including superhydrophilic ($WCA < 10$), hydrophilic ($10 < WCA < 90$), hydrophobic ($90 > WCA > 150$), and superhydrophobic ($WCA > 150$) surfaces (Ref 1–3). The major factors that influence the wetting behavior are surface chemistry and surface topography (Ref 4–8). T. Young (Ref 4) described the wetting behavior of a smooth solid surface and the effect of the surface free energy (SFE) on the contact angle. The wetting behavior of rough surfaces is commonly referred to the Wenzel model (Ref 5), Cassie–Baxter model (Ref 6) or their combination (Ref 8). Depending on the WCA and chemical, physical, and mechanical properties, the surfaces with specific wetting behavior are used in various applications including self-cleaning (water droplets collect the dust particles while sliding off a surface), water–oil separation (superhydrophobic-superoleophilic surface repel water and attract oil), anti-biofouling (reduced area of a solid–liquid interface hinders growth of microorganisms), etc. (Ref 9–14). A particular attention is focused on potential application of robust hydrophobic and superhydrophobic surfaces made of rare earth oxides (REOs) and some other hard materials, such as cermets (i) in heat transfer systems to provide drop-

Electronic supplementary material The online version of this article (<https://doi.org/10.1007/s11666-020-01130-6>) contains supplementary material, which is available to authorized users.

✉ Pavel Komarov
pavel.komarov@ceitec.vutbr.cz

¹ CEITEC – Central European Institute of Technology, Brno University of Technology, Purkyňova 123, 612 00 Brno, Czech Republic

² AdMaS Center, Faculty of Civil Engineering, Brno University of Technology, Purkyňova 139, 612 00 Brno, Czech Republic

wise condensation that significantly (up to 10 times) improves heat transfer performance than film-wise condensation typically appearing on currently used hydrophilic stainless steel (Ref 15, 16); (ii) for anti-icing behavior of ship parts and off-shore platforms, etc., in which case the high value of WCA and low water sliding angle could minimize ice adhesion (Ref 17–20); (iii) to enhance the corrosion resistance, as with increasing WCA, the area of contact of a solid surface with a corrosive liquid (water) is decreased (Ref 21); (iv) in pipes, submarines and ships as drag-reduction surfaces (e.g. muddy water transportation), where low adhesion reduces energy losses during the liquid transport (in pipes) or the movement of the parts of ships/submarines (Ref 22); (v) to increase the cavitation erosion resistance, since the superhydrophobic surfaces typically have reduced drag in laminar and turbulent flow and relatively high corrosion resistance (Ref 23).

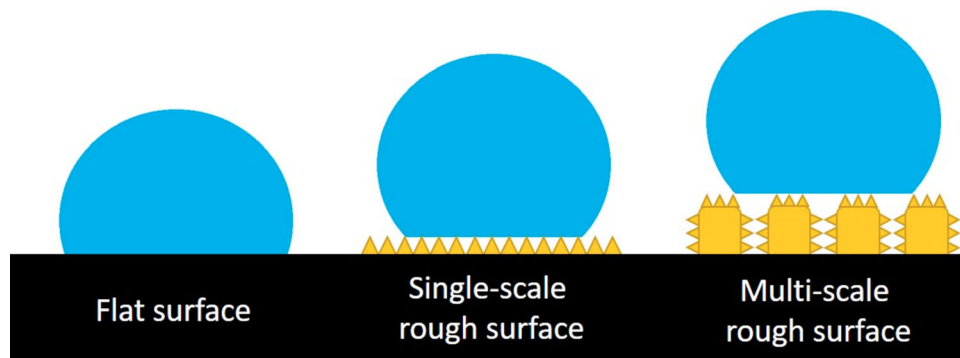
Commonly used ceramic and metallic surfaces are hydrophilic due to their high surface free energy; only the REOs provide hydrophobicity in the polished state that is attributed to their unique electronic structure (Ref 24). Regardless of the material, to obtain the superhydrophobic state of the surface with the so-called lotus effect (Ref 1–3), the formation of a multi-scale surface roughness is required (Ref 7, 25), Fig. 1 (Ref 25).

Currently, there are many technologies used to obtain a specific wetting behavior based on a combination of unique multiscale topographies and low surface energy materials (Ref 9–11, 26–28). Nevertheless, all used technologies have some major disadvantages that limit their application on large industrial scale, such as time-consuming process or constraints on size and shape of treated components due to the limited size of the required vacuum/inert atmosphere chamber, the insufficient mechanical stability (e.g. the low wear resistance of fluoropolymers (Ref 27)), or high technology costs associated with the high price of rare earth element oxides and/or even higher price of their precursors (Ref 29–31). Therefore, the inexpensive, fast, and industrially scalable technology for the manufacture of

mechanically stable surfaces with a specific wetting behavior is remaining challenging.

For these reasons, thermal spray technologies are of a great interest, as they are widely spread scalable technologies for preparation of coatings based on different material combinations (ceramic, metallic, composite and polymer materials) and with tailored properties (e.g. wear resistance, corrosion resistance, etc.). Several efforts to produce highly hydrophobic or superhydrophobic coatings by thermal spraying of hard ceramic and cermet materials combined with subsequent chemical treatment were undertaken. For instance, Sharifi et al. (Ref 28) obtained superhydrophobic behavior of TiO_2 suspension plasma sprayed coatings by additional immersion into stearic acid solution, with WCA above 155° . Atmospheric and vacuum solution precursor plasma spraying of REOs generated superhydrophilic/hydrophilic as-sprayed coatings that turned into superhydrophobic after vacuum treatment for 12 h (Ref 30, 31). Such transition of wettability was explained by the formation of a low surface energy film of hydrocarbons during vacuum treatment (Ref 31). However, the coatings lost their superhydrophobicity after subsequent heat annealing at 250°C (Ref 30). The investigation of the wetting behavior of WC cermet coatings produced by high velocity oxy-fuel (HVOF) and air-fuel (HVOF) was also reported. For instance, Xi et al. (Ref 32) fabricated WC-Co coatings with WCA of $123 \pm 2.3^\circ$ in the as-sprayed state. After surface modification by hydrophobic nano- SiO_2 , the water contact angle increased up to $154.3 \pm 3.0^\circ$ and the coatings showed steady anti-icing performance (Ref 32). In the paper by Qiao et al. (Ref 33), polished hydrophilic HVOF WC-Co-Cr coatings developed for diamond drill bits used in the oil exploitation were laser-textured, which improved water repellency and provided hydrophobicity (WCA up to 136.5°). Vijay et al. (Ref 34) investigated wettability of different HVOF WC-Co-Cr coatings. Their coatings exhibited a relatively high WCA, from 114° to 135.1° in the as-sprayed state, that the authors connected to fine carbides contained in the feedstock powder that

Fig. 1 Schematic illustration of wetting behavior of surfaces with a different surface roughness adapted from (Ref 25)



formed fine features on the coating surface thus providing hierarchical/multi-scale surface roughness (Ref 34).

In our previous study on this topic (Ref 35), the wetting behavior of atmospheric plasma sprayed WC-based wear-resistant cermet coatings was investigated, showing slightly hydrophobic behavior in both the as-sprayed and polished states. Unfortunately, the stability of WCA was found to be insufficient due to the relatively high porosity of produced coatings and gradual penetration of the liquid into the pores. Therefore, high velocity oxy-fuel spraying was chosen in this study to lower porosity and due to some other advantages, such as higher hardness and higher efficiency and mobility of the equipment. The WC-Co-Cr cermet coatings were produced from three different powders (coarse, coarse with ultrafine WC and fine with ultrafine WC) by HVOF. The main idea was to develop hard cermet coatings with multi-scale surface features, which can lead to the hydrophobic or even superhydrophobic state. Additionally, recent studies focusing on HVOF cermet coatings with different WC particle sizes revealed that ultrafine WC particles can provide very high hardness and good mechanical properties (Ref 36), lower oxidation during wear testing (Ref 37), higher corrosion resistance in 3.5% NaCl environment (Ref 38) and higher wear resistance (Ref 39, 40) in comparison to conventional WC feedstock. The water contact angle and surface free energy were obtained by the sessile droplet method for both the as-sprayed and polished coatings to study the influences of surface chemical composition and surface topography. Furthermore, the coatings were modified by the silicone oil (polydimethylsiloxane) as the well-known hydrophobic agent in order to (i) improve water repellency and to (ii) isolate the effect of surface roughness on wettability. The Wenzel, Cassie–Baxter and combined models were employed to describe the wetting behavior. To evaluate the robustness of hydrophobicity, long-term slurry abrasion testing was performed on as-sprayed and as-sprayed modified samples.

Experimental Procedure

Spraying of Cermet Coatings

Three commercial agglomerated and sintered WC-Co-Cr powders, GP10C-16, GP10CU-16, and GP10CU-31 (XTC, China), with different particle size distributions (coarse or ultrafine WC particles dispersed in Co-Cr metallic matrix) were used to produce three series of cermet coatings. Morphology of the feedstock powders, which was studied using scanning electron microscopy (SEM; LYRA3, TESCAN, Czech Republic) in backscattered electron (BSE) mode, is shown in Fig. 2. The coatings, henceforth

designated as C16, CU16, and CU31, respectively, were prepared by HVOF spraying using a GLC5 gun (GTV, Germany) installed on a six-axis IRB 2600 robot (ABB, Germany). AISI 304 stainless steel coupons (30 mm x 10 mm) with a NiCr (Amperit 251, Höganäs AB, Germany) HVOF-sprayed bond coat ($\sim 150 \mu\text{m}$ in thickness) were used as substrates. The NiCr bond coat was employed to improve the adhesion of cermet coatings, based on our previous experimental experience with such systems. Prior to spraying of the bond coat, the stainless steel substrates were grit blasted with alumina particles and cleaned in an ultrasonic bath to remove contaminants. The substrate temperature was kept at 30–40°C before each spraying run. An AccuraSpray G3C system (Tecnar Automation, Canada) was utilized to record in-flight temperature and velocity of powder particles at the moment of impact onto the substrate surface. The information on the feedstock powders, HVOF spraying parameters, and particle in-flight behavior are summarized in Table 1.

Sample Surface Preparation

Each type of experimental WC-Co-Cr cermet coating was studied in four different surface states, namely in the as-sprayed state, after polishing, and in the as-sprayed and polished states with silicone oil surface modification. These states are henceforth labeled as AS, P, AS-M and P-M, respectively. Polishing was performed using diamond pastes, starting from 9 μm down to 1 μm abrasive particles, until the surface root mean square height S_q lower than 0.20 μm and the surface roughness factor R_s below 1.01 were obtained. The polished samples were prepared in order to eliminate the influence of surface topography and thus to compare the effect of different phase compositions on wetting behavior and surface free energy values.

Concerning the superhydrophobic surface modification, a simple method of spraying of a hydrophobic agent by a spray pump was applied. The commercially available silicone oil (Novato, Czech Republic) with polydimethylsiloxane (PDMS) basis was chosen in this study due to its low price and availability. The oil was sprayed onto the coating surfaces from the distance of 300 mm under the angle of 90°. Subsequently, these modified samples were put under the vacuum of 1×10^{-1} Pa pressure to let the oil penetrate into the coating and fill the pores. Following that, the samples were heat treated in a furnace at 350°C for 30 min. After curing, a very thin transparent layer was present on the surface, which did not noticeably change surface topographical features. The silicone oil surface treatment was used with the aim to, firstly, provide superhydrophobic behavior, and secondly, to eliminate the influence of initial surface chemistry, thus isolating the topography effect.

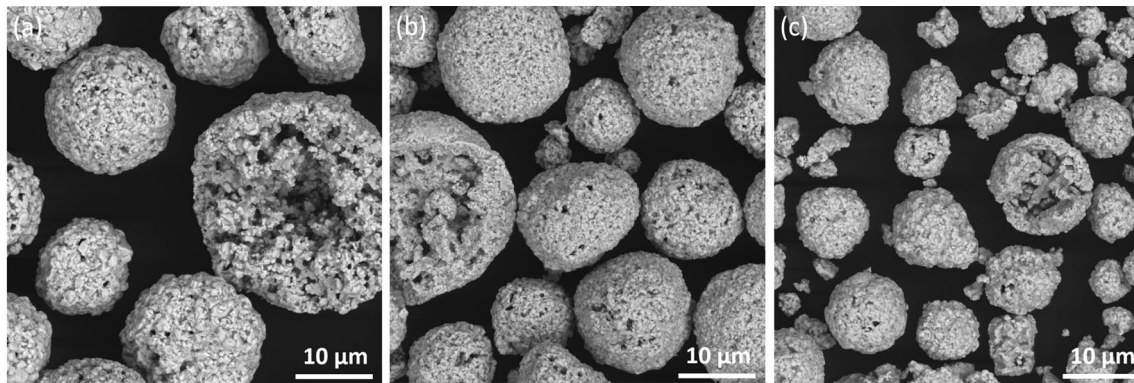


Fig. 2 Morphology of the feedstock powders (a) GP10C-16, (b) GP10CU-16, and (c) GP10CU-31 (SEM BSE)

Table 1 Feedstock powder and coating spraying parameters

Coating designation	C-16	CU-16	CU-31
Feedstock powder	GP10C-16	GP10CU-16	GP10CU-31
Powder chemical composition, wt%	86WC-10Co-4Cr		
Agglomerate size, µm	– 25 + 5		– 10 + 2
WC carbides size, µm	> 0.5	< 0.5	
Ethylene, slpm	96		
Oxygen, slpm	252		
Spraying distance, mm	200		
Robot movement speed, mm/s	600		
In-flight particle velocity, m/s	~ 610	~ 615	~ 680
In-flight particle temperature, ° C	~ 2200	~ 2130	~ 2020

Coatings Characterization

The cross-section microstructure and the surface appearance of prepared cermet coatings were studied using a scanning electron microscope LYRA3 (Tescan, Czech Republic) equipped with an energy dispersive x-ray spectrometer XFlash 5010 detector (Bruker, USA). Cross-section micrographs, 1 mm² in size obtained at 700 × magnification, were used to estimate the porosity, using the open source ImageJ software. Phase composition was evaluated using a Rigaku SmartLab 3 kW diffractometer (Rigaku, Japan) set up in the Bragg–Brentano geometry with Cu K α radiation ($\lambda = 0.154$ nm) operated at the current of 30 mA and voltage of 40 kV. The diffraction patterns were collected from 20 to 90° with the step size of 0.02° and the scan step time of 1 s. The Rietveld refinement of the obtained x-ray diffraction (XRD) patterns was performed using the X’Pert Highscore v.3a software and the crystallographic models from the International Crystallographic Database of detected phases, i.e. WC (ICSD No 01-072-0097), W (ICSD No 01-089-3012) and W₂C (ICSD No 98-007-7568). To estimate the crystallinity of experimental samples, the method of a “constant background intensity” was used in the Highscore v.3a software.

In this method, the crystallinity C [%] is determined by Eq 1:

$$C = \frac{100 * \sum I}{\sum I_{total} - \sum I_{const.bgr.}} \quad (\text{Eq 1})$$

where $\sum I$ is the area of crystalline peaks, $\sum I_{total}$ is the total area and $\sum I_{const.bgr.}$ is the area of constant background, which is subtracted from the total intensity (Ref 41).

As the wetting of the flat solid surface depends on the chemistry of the very surface layer, x-ray photoelectron spectroscopy (XPS) of C16, CU16 and CU31 polished unmodified samples was performed to analyze the elemental composition and chemical bonding state of the elements. Prior to the XPS analysis, the samples were cleaned in an ultrasonic bath with isopropyl alcohol and dried by hot air, which is the same procedure as in the case of WCA and SFE measurements.

XPS analysis was performed at a Kratos Analytical Axis Supra (KRATOS-XPS, Kratos Analytical Ltd., UK) spectrometer with a monochromatic Al source using a pass energy of 80 eV for wide spectra and of 20 eV for high-resolution analysis of C 1 s, O 1 s, W 4f, Co 2p and Cr 2p peaks. The analyzed regions were 300 × 700 µm² in size. The deconvolution of mentioned peaks was carried out in the CasaXPS 2.3.22PR 1.0 software, applying synthetic

peak models and constraints supported by the existing literature (Ref 42–46).

The surface topography was measured by a LEXT OLS 4100 (Olympus, Germany) laser scanning confocal microscope. The topography was characterized by the surface arithmetic mean height (Sa), the root-mean-square height (Sq), the skewness (Ssk), the kurtosis (Sku) and the surface roughness factor (Rs) to assess their correlation with wetting behavior. Five regions of size of $\sim 640 \mu\text{m}^2$ were evaluated on as-sprayed and polished surfaces in both unmodified and modified states.

The surface arithmetic mean height Sa and the root-mean-square height Sq , which are the areal analogs of widely used profile arithmetical mean height (Ra) and profile root mean square height (Rq), provide the information on the vertical extension of a surface. The skewness reveals if the surface has predominantly high peaks ($Ssk > 0$) or deep valleys/pores ($Ssk < 0$) (Fig. 3a). The kurtosis characterizes the sharpness of peaks and valleys ($Sku > 3$) or their flatness ($Sku < 3$) (Fig. 3b). The complexity of surface topography can be described by the developed interfacial area ratio Sdr , which is defined in the ISO 25178-2 standard (Ref 47) and was found previously to correlate well with wetting behavior of cermet coatings (Ref 34). In this study, the surface roughness factor Rs is preferred instead, because it appears in Wenzel (Ref 5), and the combined Wenzel–Cassie–Baxter (Ref 8) models of wetting discussed in section “Wetting Behavior and Surface Free Energy”. This parameter is defined as the ratio of the “true” surface area and its projection and the relationship between Sdr and Rs is thus $Rs = Sdr + 1$ (Ref 48).

Wetting Behavior and Surface Free Energy Measurements

The water contact angle and surface free energy measurements of experimental samples in four different states (AS,

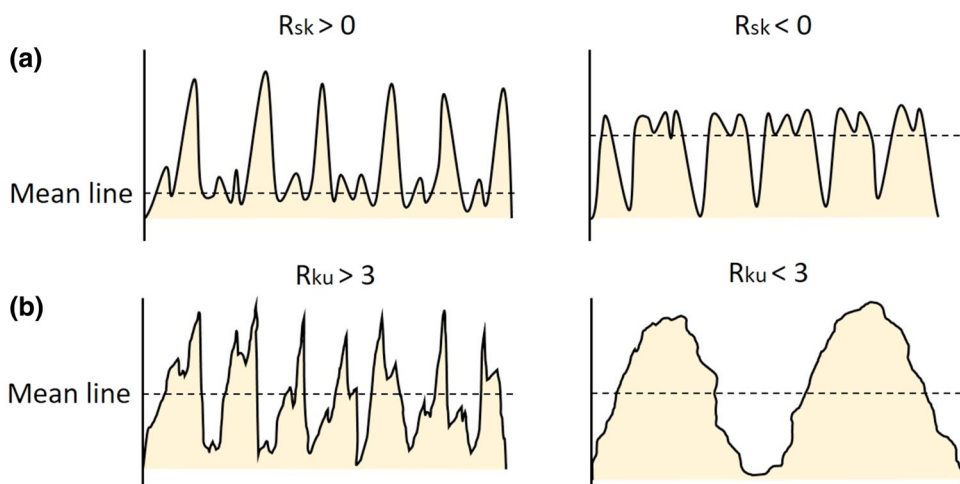
P, AS-M, and P-M) were conducted by the sessile droplet method using a Surface Energy Evaluation System device (See System E, Advex Instruments, Czech Republic) with a proprietary image analysis software. The measurements were performed at the room temperature on the same day the coatings were sprayed. Before measurements, the samples were thoroughly cleaned in an ultrasonic bath with isopropyl alcohol and dried by hot air to remove extra impurities from the surface. The $3 \mu\text{l}$ droplet of liquid was deposited onto the solid surface, and the angle made by intersection of the gas–liquid interface and the solid–liquid interface was estimated. Small droplets were used to decrease the influence of gravity on the shape of the droplets.

Assessment of the wetting behavior of a smooth solid surface by the sessile droplet method is based on the Young’s Eq 2, in which the liquid surface tension γ_{lv} , the solid surface free energy γ_{sv} (SFE), the solid/liquid interfacial free energy γ_{sl} , and the contact angle θ_Y terms are included (Ref 4):

$$\gamma_{sv} - \gamma_{sl} = \gamma_{lv} * \cos \theta_Y. \tag{Eq 2}$$

The calculation of the surface free energy was carried out using the Owens–Wendt theory via measuring the contact angles of water and diiodomethane liquids (Ref 49, 50). The Owens–Wendt theory considers the surface free energy as a sum of polar (γ^P) and dispersive (γ^D) parts. According to this theory, the polar part of a liquid will interact with the polar part of a solid, while the dispersive part of a liquid will interact with the dispersive part of the solid, respectively. The theory assumes that the liquid with high polarity (e.g. water) will spread on a polar solid surface resulting in a low contact angle due to stronger polar–polar interaction. If the dispersive part of a solid surface is larger, then the contact angle will be higher due to weaker polar–polar interaction. Diiodomethane as a liquid with a low polar part ($\gamma^P \sim 0 \text{ mJ/m}^2$) and water as a liquid with a

Fig. 3 Schematic illustration of profiles with different (a) skewness R_{sk} and (b) kurtosis R_{ku} ; R_{sk} and R_{ku} are profile analogs of S_{sk} and S_{ku}



high polar part ($\gamma^P = 51 \text{ mJ/m}^2$) were chosen to properly evaluate the surface free energy.

At least 10 droplets of each liquid were evaluated on each sample. The droplets were set on the regions which were earlier selected for roughness measurements (section “Coatings Characterization”). To evaluate the water mobility, measurements of the sliding angle (SA) on modified surfaces were done via tilting the sample with larger water droplets ($10 \mu\text{l}$) until the droplet started moving. Larger droplets were used in this case to provide sufficient weight.

The CU16 coating, with the highest water mobility, was chosen for the preliminary self-cleaning and muddy water transportation tests. During the self-cleaning test, the sample was covered by fine alumina powder and then tilted by 10° . Water droplets ($\sim 10 \mu\text{l}$) were set on the surface to roll off and collect the alumina powder during descent. The muddy water transportation test was carried out via setting continuous flow of a suspension of water and WC powder particles over the surface tilted by 10° .

Theoretical Models of Wetting Behavior of Rough Surfaces

As the roughness is not considered by the Young’s Eq 2, the Wenzel model (Ref 5), Cassie–Baxter model (Ref 6) or combined model (Ref 8) were applied to describe the roughness effect. The Wenzel model (Fig. 4) assumes that the liquid droplet penetrates the grooves (valleys) of a solid surface. According to this model (Eq 3), the roughness factor R_s amplifies the wettability in comparison to the polished state (Ref 5). It means that if the polished surface is hydrophilic ($\text{WCA} < 90^\circ$), it will become more hydrophilic ($\text{WCA} \ll 90^\circ$) in a rough state.

$$\cos \theta_W = R_s * \cos \theta_Y \quad (\text{Eq 3})$$

On the other hand, the Cassie–Baxter wetting model (Fig. 4) assumes that there is a layer of air pockets trapped between the peaks or inside the pores that prevents the contact of the liquid with the solid surface, thus increasing water repellency. According to Cassie–Baxter model (Eq 4), the wettability further depends on the fraction area of solid surface (f_s) that is in contact with water (Ref 6):

$$\cos \theta_{CB} = f_s * \cos \theta_Y + f_s - 1 \quad (\text{Eq 4})$$

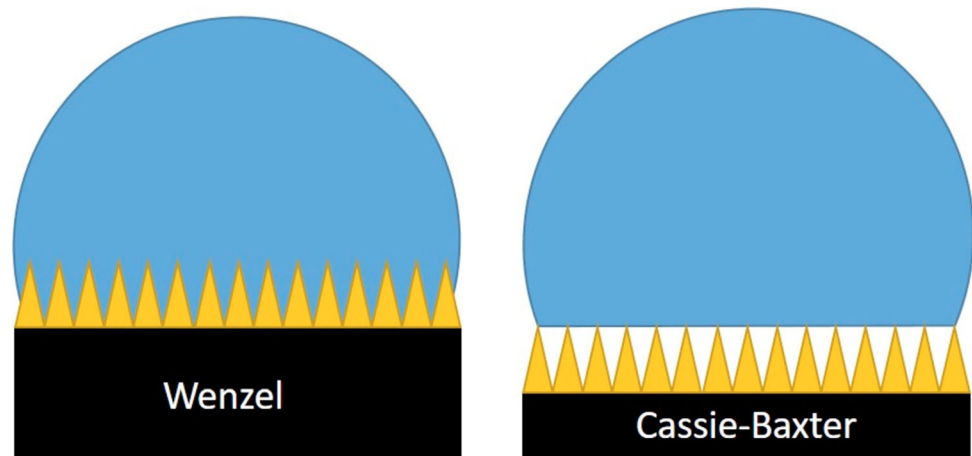
The combined model was found to be useful in description of wetting behavior of solid surfaces with multi-scale roughness (Ref 8). Considering the roughness factor R_s of the solid surface area that is in contact with a liquid, the modified form of the Cassie–Baxter equation is derived as:

$$\cos \theta_{CBW} = R_s * f_s * \cos \theta_Y + f_s - 1 \quad (\text{Eq 5})$$

Slurry Abrasion Response test

To estimate the robustness of wetting properties, the as-sprayed and as-sprayed modified C16 and CU16 (most hydrophobic) coatings were subjected to the Slurry Abrasion Response (SAR) test (ASTM G75-15 standard) (Ref 51). During the test, the specimens were immersed into the bath with the suspension of artificial seawater (ASW) and solid Al_2O_3 particles (50% wt.) with the rubber stripes on the bottom; the specimens were pressed against the rubber with the force of 22.24 N per sample and were moved along the rubber by an electro engine. The duration of the test of as-sprayed samples was 4 h, corresponding to 11,520 cycles. The WCA and topography changes were evaluated after the test. The testing of as-sprayed modified samples was interrupted after 1 min (48 cycles) because of the loss of the benefits of the modification layer.

Fig. 4 Wetting behavior of a rough surface with Wenzel and Cassie–Baxter regimes of wetting



Results and Discussion

Microstructure and Chemistry of the Coatings

The EDX analysis of as-sprayed unmodified samples revealed the presence of W, C, O, Cr, and Co peaks, Table 2. The analysis of as-sprayed modified samples revealed the additional peak of Si (~ 10 wt.%) that is supposed to come from the silicone oil. The distribution of elements was nearly equal among the coatings and was in agreement with the literature (Ref 52).

Figure 5 shows the comparative XRD patterns of C16, CU16 and CU31 as-sprayed unmodified coatings. The presence of WC, W and W_2C phases was clearly detected; however, the peaks of crystalline Co and Cr binders were not observed. Intensity values of WC, W_2C and W phases of C16 and CU16 coatings were similar and differed from the CU31 coating. This is also obvious from the Rietveld quantification results collected in Table 3 that revealed the highest decarburization of WC to W_2C and W in the CU31 coating and the highest content of the retained WC phase in the C16 coating. Clearly, the level of decarburization is mainly related to the size of the powder particles and the CU31 coating, which was prepared from the finest feedstock powder, shows the highest decarburization, even though the temperature of particles at the stand-off distance (200 mm) was the lowest. The fine powder particles in the feedstock material were observed to achieve higher decarburization levels also in some previous studies (Ref 36, 39, 53) and thus the lower temperature of CU31 particles measured at the stand-off distance is believed to be caused by their tendency to travel outside the flame core with increasing distance, cooling more than the coarse C16 and CU16 particles. Such conclusion is supported by the computational analysis reported by Li et al. (Ref 54), in which case the highest temperature was predicted for particles with the diameter of 20 μm while smaller (and also larger) particles achieved lower temperatures, which was explained by high sensitivity of small particles to fluctuations of the gas flow during HVOF spraying.

In all the coatings, the XRD amorphous halo (approximately from 34° to 45° 2θ values) indicated the presence of

amorphous or nano-crystalline phases. The amorphous halo is associated with Co and Cr binders and its presence agrees with the literature. The crystallinity content increased with decreasing feedstock particle size, from the C16 coating (coarse powder and coarse WC particles) to the CU31 coating (fine powder and ultrafine WC particles), see Table 3. This can be explained by the difference in the powder particle in-flight temperature at the moment of impact (Table 1), which was about 2200°C for the C16 coating, compared to 2020°C for the CU-31 coating. Such high temperature could promote formation of amorphous/nano-crystalline phases due to very fast cooling of molten and semi-molten powder particles impacting the cold substrate (Ref 39, 53, 55–58).

The XRD patterns of modified samples did not reveal any differences in comparison with the unmodified ones. The presence of the silicone oil was not detected, probably due to the very low thickness of the modification layer.

The quantitative results of XPS analysis performed on polished unmodified samples are shown in Table 4. High-resolution XPS spectra of O 1s and W 4f peaks are presented as Fig. 6. No clear peaks of Co 2p and Cr 2p were detected and thus data on these elements are not presented.

The content of W in the analyzed samples was much lower than what was reported by Wesmann et al. for their WC-Co-Cr HVOF samples (Ref 42, 43) but it should be noted that Ar sputtering was used prior to the XPS measurements in their experiment, which reduces the amount of oxides, as also noted by the authors (Ref 42, 43). The O 1s and W 4f deconvoluted peaks revealed the difference in W–O content among the samples. Besides the oxygen O 1s peak at ~ 532 eV that can be associated with the organic C–O contamination from the atmosphere, the second O 1s peak at ~ 530 eV is related to the metal oxides, in our case tungsten oxides. The analysis of W 4f spectra showed the presence of W–C composition with peaks at ~ 31.5 and ~ 33.5 eV and W–O composition with peaks at ~ 36 and ~ 38 eV. The content of W–O increased from the C16 sample to the CU31 sample. The surfaces with a higher content of W_2C and/or W have a higher W–O content, which is related to the instability of W_2C and formation of tungsten oxides in atmosphere (Ref 44). The same trend was observed in the present work; the C16 sample with the lowest decarburization showed the lowest W–O content in the XPS spectra and the CU31 sample with the highest decarburization showed the highest W–O content. With increasing intensities of W–O, from the C16 sample to the CU31 sample, the atomic percentage of O 1s and W 4f is increased as well, Fig. 6 and Table 4.

The deconvolution of C 1s spectra, Fig. 7, showed nearly the same results for all the samples, with the main peak at ~ 283 eV that is related to the WC compound. The only difference was the second peak at ~ 285 eV in

Table 2 Elemental analysis of as-sprayed coatings

Coating	Element, wt.%				
	W	C	O	Cr	Co
C16	79.6	11.6	3.1	0.2	5.5
CU16	80.1	10.8	3.4	0.9	4.8
CU31	78.3	12.3	4.6	0.3	4.5

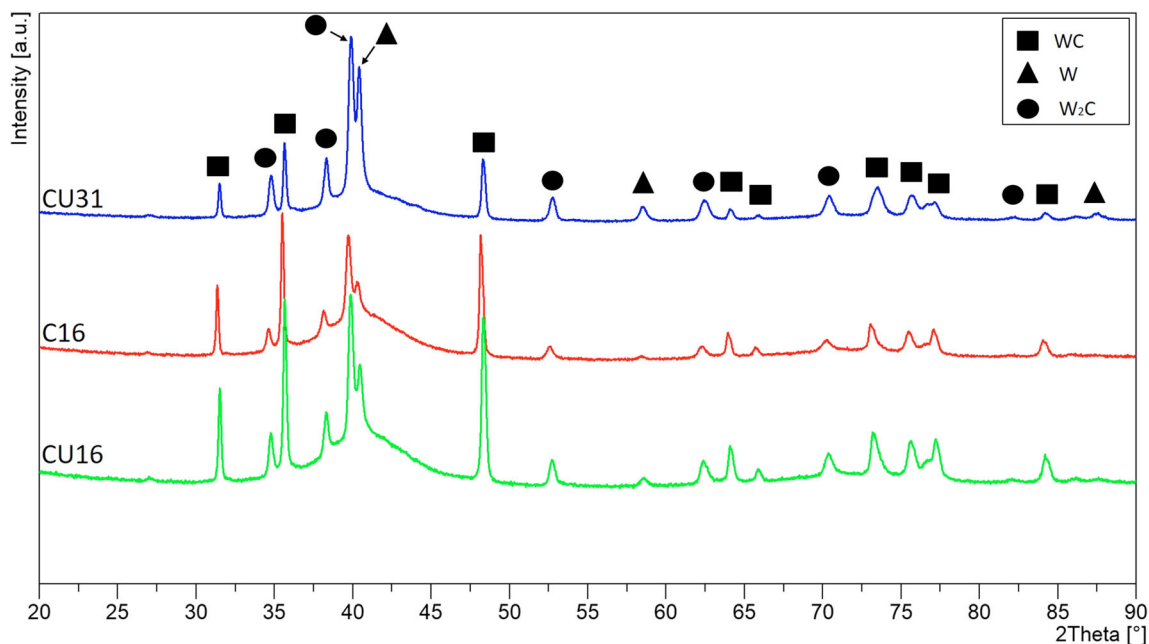


Fig. 5 X-ray diffraction analysis of C16, CU16 and CU31 unmodified samples

Table 3 Percentage of crystalline phases and crystallinity content in the coatings

Coating	Phase content, wt. %			Crystallinity content, %
	WC	W ₂ C	W	
C16	51	37	12	36
CU16	49	39	12	41
CU31	20	54	26	50

Table 4 XPS quantitative analysis of polished unmodified samples

Coating	Element, at. %		
	O 1s	C 1s	W 4f
C16-P	28.7	63.6	7.7
CU16-P	33.4	53	13.6
CU31-P	36.2	48.5	15.3

the CU31 sample that is related to the C-H hydrocarbon compound.

Figure 8 shows representative cross-sectional images of C16, CU16 and CU31 coatings. Micrographs revealed dense splat-like microstructure that is typical for HVOF sprayed coatings (Ref 39, 53, 55–57). The porosities were ~ 1% for CU31 and ~ 1.5% for C16 and CU16 samples. As expected (Ref 53, 57, 58), the lowest porosity was measured for the CU31 coating produced from the finest powder. The high-magnification micrographs (Fig. 8b, d, f) expose the differences in carbides size and

morphology among the samples. The C16 coating prepared from the coarsest powder predominantly contained irregularly shaped carbides with the size above 1 μm . In contrast, the coatings CU16 and CU31 prepared from the powder feedstock with ultrafine carbides showed large amount of carbides with the size below 1 μm and with rounder morphology that indicates full or partial melting of the carbide particles during spraying.

Topography

Surface topography characteristics were evaluated for all the samples. In the case of polished samples, topographical measurements were carried out to assure Sq lower than 0.20 μm and Rs below 1.01. Furthermore, the analysis of modified samples showed no changes in roughness parameters and, therefore, only the as-sprayed coatings are discussed in the following text.

SEM images of surfaces after spraying are presented in Fig. 9 and the height maps are shown as Fig. 10. All coatings had the multi-scale surface roughness composed of the large-scale waviness surface component related mainly to the deposition process (Ref 48), micron-sized peaks and valleys of the lateral size of 2–10 microns and, finally, fine WC carbide particles, hundreds of nanometers in size, which significantly increase the surface area. We connect such a unique multi-scale structure with sintered and agglomerated feedstock powder with fine carbides that created nano-scale features on a rough surface of the splats.

The surface arithmetical mean height Sa and the surface root mean square height Sq increased with the decreasing

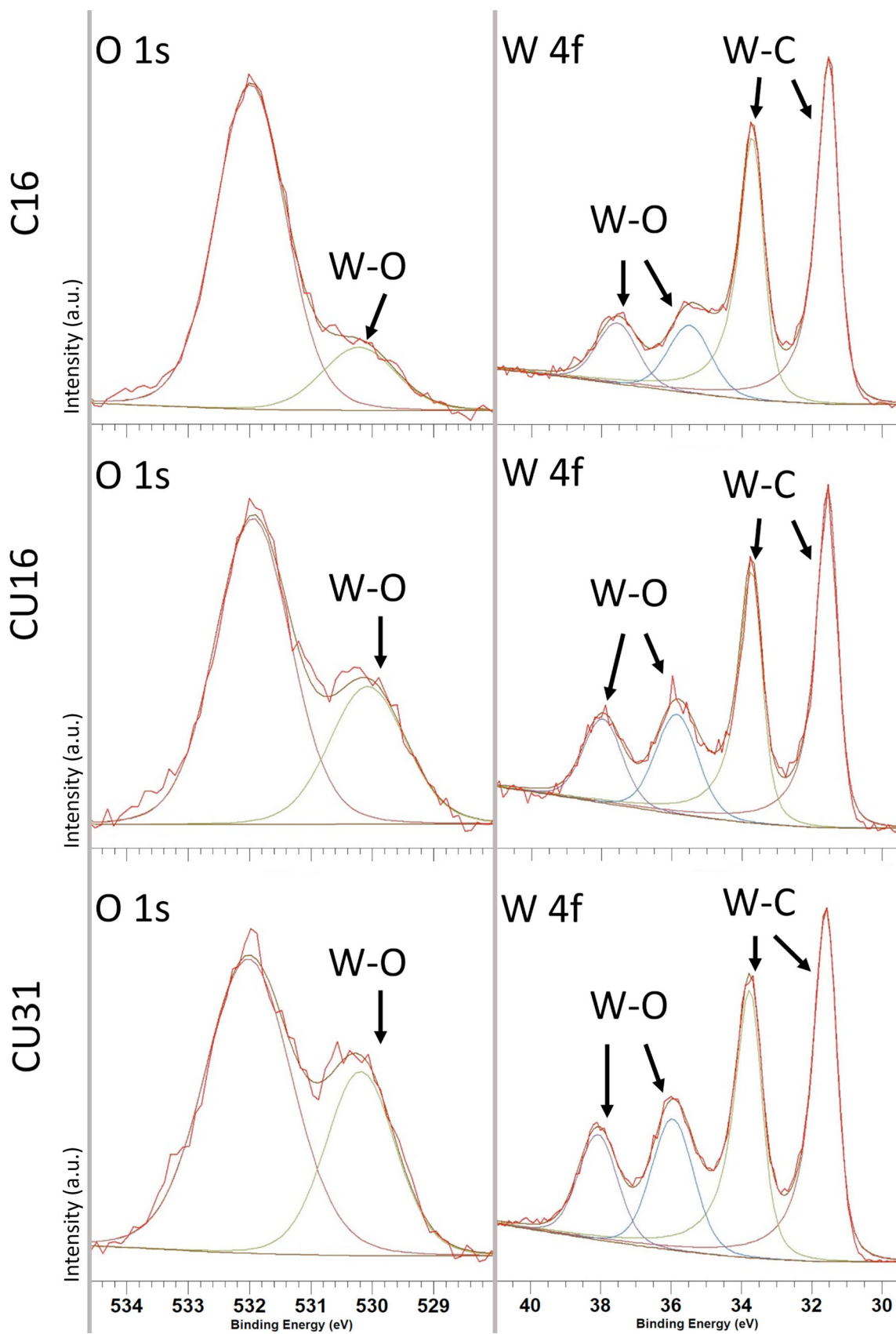


Fig. 6 High-resolution XPS spectra of O 1s and W 4f peaks from polished unmodified samples

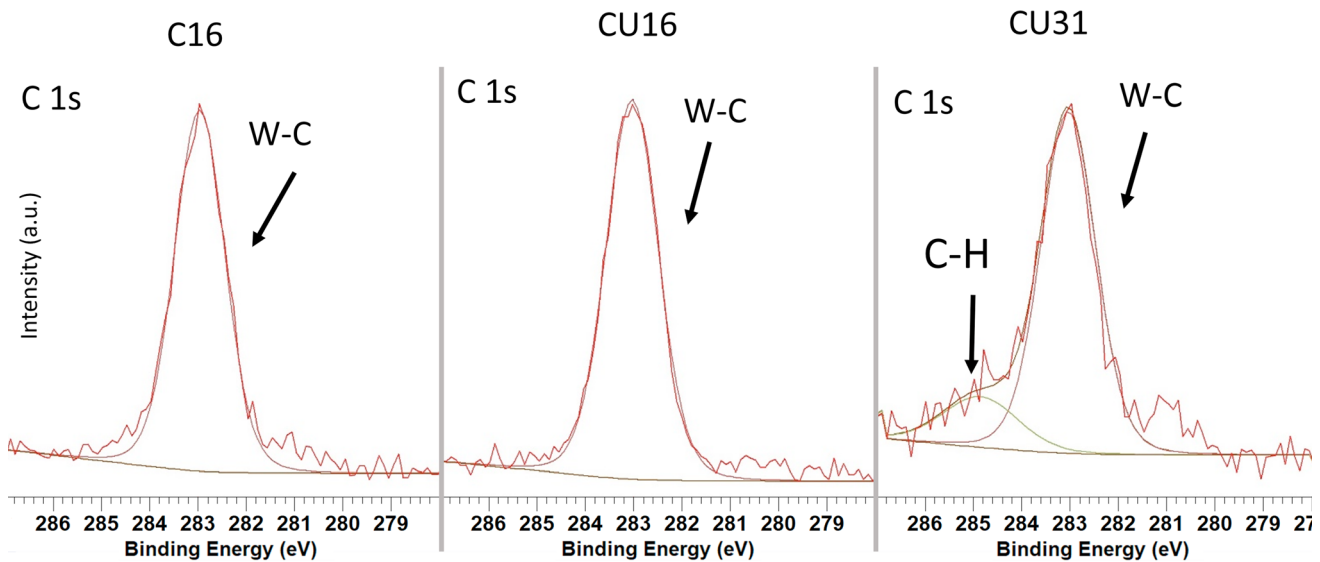


Fig. 7 High-resolution XPS spectra of C 1 s peak from polished unmodified samples

size of the feedstock powder particles, Table 5. The C16 coatings produced from the coarsest powder had the lowest Sa and Sq values, the CU16 coatings produced from the powder with ultrafine WC particles had higher values and the CU31 coatings produced from the finest powder are characterized by the highest Sa and Sq values. Al-Mutairi et al. (Ref 52) reported the same trend of increasing surface roughness with decreasing powder particles size in the case of HVOF-sprayed WC-Co coatings. Note that this behavior is opposite to what was observed for some plasma sprayed coatings (e.g. (Ref 59)) and it is most likely related to the degree of flattening, which was smaller for colder particles with lower momentum (Table 1).

The opposite trend can be seen for the skewness and the kurtosis. In the case of the skewness, there is a noticeable difference between C16/CU16 and CU31 samples, suggesting that C16/CU16 samples had more peaks than valleys/pores ($Ssk > 0$) than the CU31 sample with equally distributed peaks and valleys/pores ($Ssk \sim 0$). In the case of the kurtosis, all the samples showed different behavior. The surface of C16 sample ($Sku > 3$) mostly consisted of sharp-cut peaks and valleys, the CU16 sample's height distribution was less narrow ($Sku \sim 3$) and the surface of the CU31 sample had flattened top of the peaks and bottom of the valleys ($Sku < 3$). The difference in distribution and sharpness of peaks/valleys is also clearly observed in 3D illustration of as-sprayed surfaces; see Fig. 10.

Finally, the surface roughness factor Rs increased with decreasing size of WC particles in the feedstock powder, which is clear from the comparison of C16 and CU16 with the same size of particles and coarse and ultrafine WC). This result confirms that the addition of ultrafine WC particles enlarged the total surface area.

Wetting Behavior and Surface Free Energy

Water contact angle and surface free energy were evaluated with excluding the influencing factors, namely, the surface topography and the surface chemistry were excluded via polishing and silicone oil surface chemistry modification, respectively.

Polished and Polished Modified Coatings

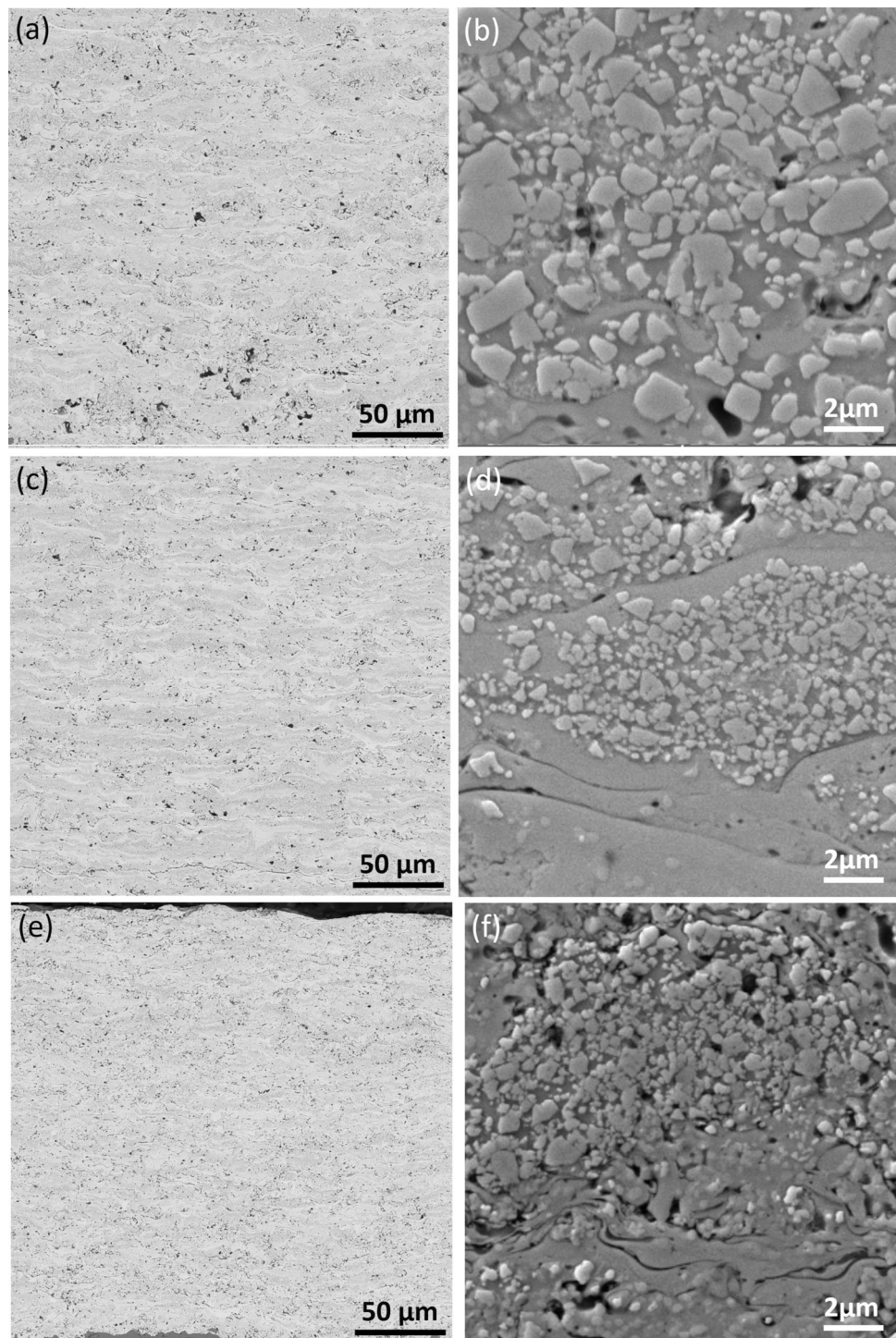
First, to understand the influence of phase composition (surface chemistry) on wettability of the three WC-Co-Cr coatings, the polished coatings ($Sq < 0.2 \mu\text{m}$ and $Rs < 1.01$) were investigated via the Young's equation (Eq 2), thus excluding the influence of surface topography on wetting behavior.

The measured water contact angle (Fig. 11) and surface free energy results are summarized in Table 6. It is observed that all the polished unmodified surfaces were hydrophilic, with the water contact angle $\sim 50\text{--}70^\circ$, and all the modified surfaces were hydrophobic, with the water contact angle of about 105° .

The data on unmodified samples agree well with the existing literature reporting the values of WCA (Ref 33) and SFE (Ref 60). It is noticeable that C16 and CU16 samples showed relatively similar water contact angles and surface free energies that differed from those of the CU31 sample. Since the roughness effect was effectively excluded by polishing, such result is primarily connected with the difference in surface chemistry.

According to the XPS analysis, the surfaces of experimental samples were mostly composed of W-O oxides and W-C carbides that are hydrophilic due to polar-polar

Fig. 8 Cross-section micrographs of (a, b) C16, (c, d) CU16 and (e, f) CU31 as-sprayed coatings

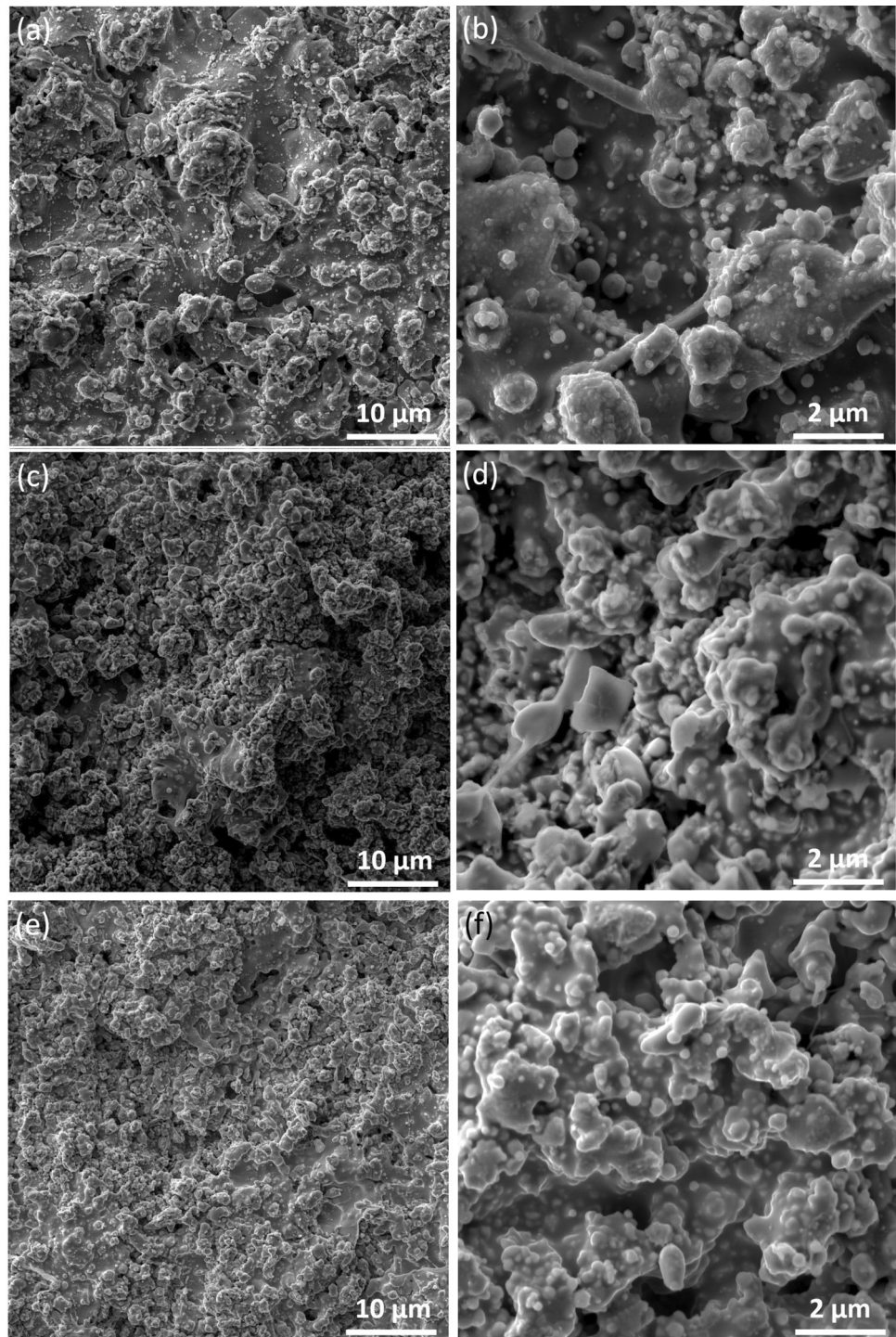


interaction with water. Only the CU31 sample showed the additional peak at ~ 285 eV in the deconvoluted C 1s spectra, that is connected to the C-H bonding. Calculations showed that the C-H peak corresponded to $\sim 10\%$ at. of the C 1s spectra in this case. Therefore, despite that all the samples were thoroughly cleaned in isopropyl alcohol prior

to XPS, WCA, and SFE analysis, some hydrocarbons could remain on the surface.

The hydrophobic effect of adsorbed nonpolar hydrocarbons was reported in numerous studies (Ref 61, 62). The metal cations have a strong electron-accepting nature and, therefore, the solid surface with a higher content of metallic phase has more chances to have adsorbed

Fig. 9 Top-view of (a, b) C16 AS; (c, d) CU16 AS and (e, f) CU31 as-sprayed coatings



hydrocarbons. The Rietveld refinement revealed the highest content of W phase in the CU31 sample (26% wt. vs. 12% wt. in C16/CU16), see Table 3, which can explain why the deconvoluted high-resolution C 1s spectra showed the presence of hydrocarbons only on the surface of the CU31 sample.

As explained above, the Owens–Wendt theoretical model (Ref 49, 50) considers the surface free energy to

consists of nonpolar (dispersive) γ^D and polar γ^P parts, which are both provided in Table 6. The contribution of polar component to the total value of SFE presented in Table 6 in the γ^P/SFE column is notably lower for the CU31 sample in comparison to C16 and CU16 samples. Based on the results of XPS analysis, we can conclude that nonpolar hydrocarbons adsorbed on the surface of W grains was primary responsible for higher WCA, lower SFE and

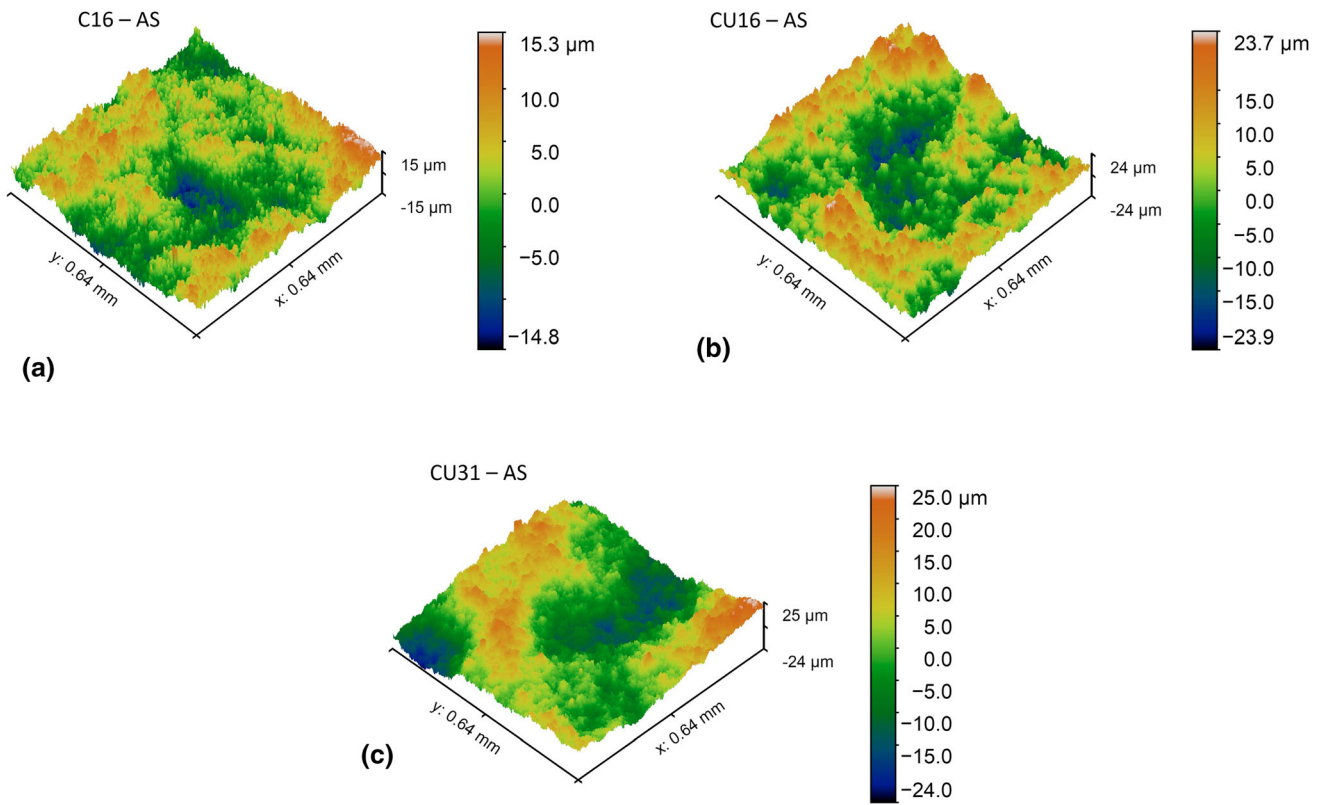


Fig. 10 Height maps of as-sprayed coatings. Note that the polished surfaces are not shown here for their flatness and similarity

Table 5 Roughness parameters of as-sprayed C16, CU16 and CU31 samples

Sample	Sa, μm	Sq, μm	Ssk	Sku	Rs
C16 AS	3.8 ± 0.5	4.9 ± 0.4	0.21 ± 0.03	4.35 ± 0.10	2.13 ± 0.01
CU16 AS	5.4 ± 0.4	6.7 ± 0.5	0.18 ± 0.01	3.03 ± 0.10	2.23 ± 0.01
CU31 AS	6.8 ± 0.4	8.3 ± 0.4	0.04 ± 0.02	2.56 ± 0.07	1.92 ± 0.02

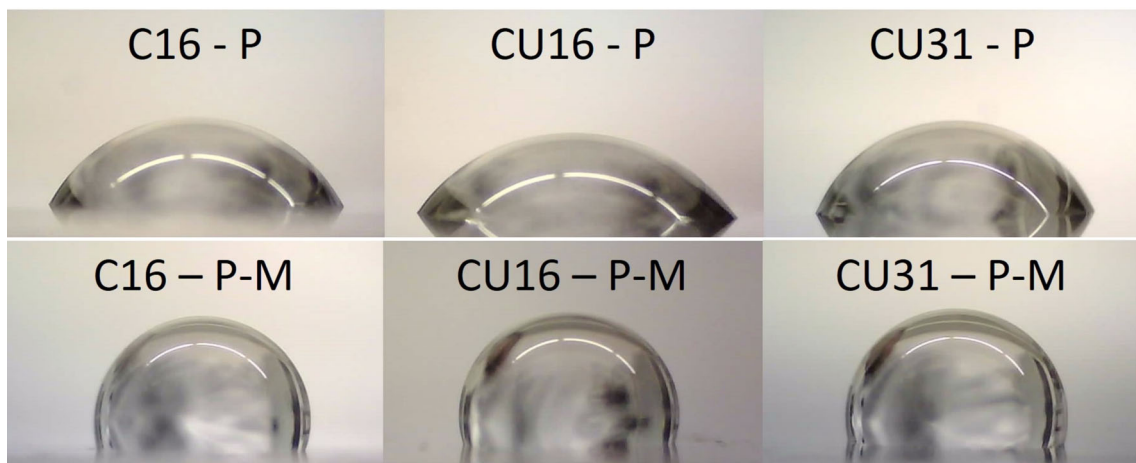


Fig. 11 Water droplet behavior on polished and polished modified coatings

Table 6 Water wetting behavior and surface free energy of polished and polished modified samples

Sample	State	WCA, °	SFE, mJ/m ²	γ^D , mJ/m ²	γ^P , mJ/m ²	γ^P/SFE
C16	P	55 ± 1	50.26	35.71	14.55	0.29
	P-M	107 ± 2	27.05	27.00	0.05	<0.01
CU16	P	53 ± 2	51.30	36.46	14.84	0.29
	P-M	106 ± 1	27.76	28.73	0.03	<0.01
CU31	P	68 ± 1	46.58	37.36	9.23	0.20
	P-M	105 ± 2	28.21	28.16	0.05	<0.01

Table 7 Water wetting behavior and surface free energy of as-sprayed and as-sprayed modified samples

Sample	State	WCA, °	Sliding angle, °	SFE, mJ/m ²
C16	AS	122 ± 3	...	17.37
	AS-M	>170	8	2.08
CU16	AS	143 ± 2	...	12.79
	AS-M	>170	5	2.10
CU31	AS	88 ± 2	...	28.49
	AS-M	152 ± 4	10	2.85

lower γ^P/SFE ratio in CU31 sample in comparison to the C16 and CU16 samples.

In the case of the modified polished state, the values of water contact angle were approximately the same (of around 105°) and the surface free energy values and the distribution of its polar and nonpolar components were also similar. Such hydrophobic wetting behavior is close to polydimethylsiloxane (PDMS) (Ref 63) that was the base of silicone oil used for the surface chemistry modification.

As-Sprayed and As-Sprayed Modified Coatings

The investigation of the wetting behavior of samples in the as-sprayed state, Table 7 and Fig. 12—top row, showed that the C16 and CU16 coatings were hydrophobic and close to the superhydrophobic state. According to our knowledge, this is the first report on the HVOF WC cermet coatings with the water contact angle above 140° in the as-sprayed state. The CU31 coating revealed a boundary “hydrophilic–hydrophobic” behavior, with the WCA close to 90°. Surface chemistry modification by oil turned all the coatings into the superhydrophobic state with low SFE, the WCA above 150° (defining condition of superhydrophobicity (Ref 1, 2)) and the sliding angle below 10°, Table 7. The best water repellency and water mobility was observed for the C16 and CU16 samples with WCA > 170° and sliding angles of 8° and 5°, respectively.

The comparison of the results of as-sprayed and polished samples shows that the roughness amplifies hydrophobicity, increases the water contact angle and

decreases the surface free energy. Furthermore, it is observed that the wetting behavior of both as-sprayed and as-sprayed modified samples does not follow the Wenzel model of wetting, but follows either the Cassie–Baxter model (Eq 4) or the combined model (Eq 5).

According to the combined model, which is appropriate for multi-scale surfaces, the increasing roughness factor R_s improves hydrophobicity and thus the high hydrophobicity of the C16 and CU16 samples in both as-sprayed and as-sprayed modified states is caused by their high surface roughness factor (2.13 and 2.23, respectively).

The f_s values obtained from Eq 5 were 4.1 (C16), 3.8 (CU16) and 23.1% (CU31) for the as-sprayed modified samples. It means that, respectively, 95.9, 96.2 and 76.9% of the interface was in fact related to the liquid–air contact, providing the superhydrophobic behavior.

On the other hand, it should be noted that both C16 and CU16 samples with the highest hydrophobicity had nearly the same positive skewness values ($Ssk \approx 0.2$, Table 5). As $Ssk > 0$ suggests that the surface is predominantly composed of peaks (Fig. 9 and 10), we assume that such property might provide the Cassie–Baxter wetting state with water droplets kept on the top of the peaks. Indeed, the CU31 sample with $Ssk \sim 0$ is then supposed to be composed of equal number of peaks and valleys, with more valleys available to be filled by water, providing a combination of Wenzel and Cassie–Baxter wetting behavior and lower water contact angle.

Ultrafine internal WC carbides embedded into the metallic matrix created very fine nano-scale peaks on the surface of micrometric splats of WC-Co-Cr powder particles melted during HVOF spraying. The micron-sized peaks superimposed with nano-sized peaks and valleys/pores (Fig. 9d, e, f) led to the high surface area, providing high water repellency due to the existence of entrapped air pockets between the liquid and solid surfaces, which prevents their contact. Vijay et al. (Ref 34) reported the same effect of fine carbides on hydrophobic wetting behavior for HVAF as-sprayed cermet coatings. The experiments revealed the connection between the hydrophobic behavior of as-sprayed samples and the superhydrophobic behavior of as-sprayed modified samples and demonstrated the fact that the combination of the

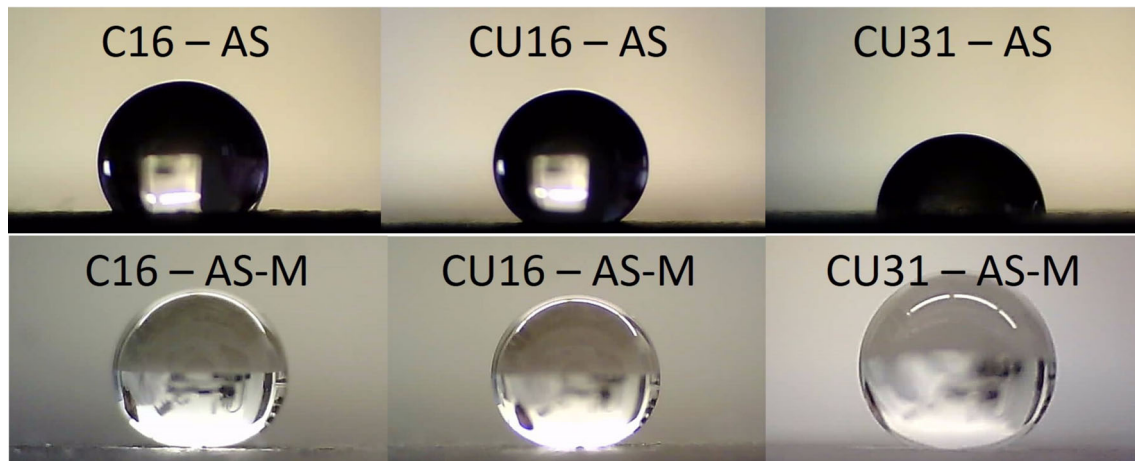


Fig. 12 Water droplet behavior on as-sprayed and as-sprayed modified coatings

unique multi-scale roughness formed by ultrafine carbide particles and surface chemistry modification can lead to superhydrophobicity of cermet coatings. In both the as-sprayed and as-sprayed modified states, the best water repellency and water mobility was shown by the CU16 sample (WCA close to 150° in the as-sprayed state; WCA $> 170^\circ$ and roll-off angle of 5° in the modified state) produced from coarse powder with ultrafine carbides. Thereby, we conclude that the combination of coarse powder and ultrafine WC particles ensures the optimal surface morphology for water repellency.

The CU16 modified superhydrophobic coating was chosen for preliminary self-cleaning and muddy water transportation tests. The Video 1 available in the Supplementary material shows that the water droplets easily rolled off the surface, collecting the alumina powder and leaving behind the clean lines on the surface. The CU16 sample presented promising durability in the muddy water transportation test as well. As demonstrated in the Video 2 of the Supplementary material, the surface remained without any contamination after the test. These preliminary observations confirm that the superhydrophobicity of the as-sprayed modified CU16 coatings is advantageous in environments with contamination.

Slurry Abrasion Response Test

The robustness of the wetting behavior was further evaluated by the SAR test of the as-sprayed and as-sprayed modified C16 and CU16 (most hydrophobic) coatings in the ASW- Al_2O_3 slurry. Figure 13 shows the water droplets on the as-sprayed coatings after the SAR test, together with the estimated WCA values. Table 8 summarizes the measured surface roughness values.

The SAR test had an impact on the surface topography and on the wetting behavior. In comparison with the initial

as-sprayed state Table 5, all roughness parameters decreased in both samples. This was the result of wear damage to the surface by abrasive Al_2O_3 particles at the peaks, which are the points of contact. The surface roughness factor that appears in the wetting models decreased by $\sim 35\%$ in both cases. On the other hand, the decrease in WCA in both samples was smaller, namely from 122° to 118° for C16 and from 143° to 128° for CU16 coatings.

The decrease in roughness is due to the flattening of the peaks, nevertheless, the SAR test produced also new surface irregularities in the form of wear tracks, which are well seen in Fig. 14 and are below the resolution of the employed laser scanning confocal microscope. Furthermore, it is clear that the fresh WC particles, which are incorporated into the matrix (Fig. 8), were exposed during the test. The presence of the wear tracks and WC particles on the surface explains relatively high WCA values measured after the SAR test and proves that the water wetting behavior of the WC-Co-Cr coatings is sufficiently robust even for sacrificial applications.

On the other hand, the SAR test of the C16 and CU16 as-sprayed modified samples revealed that the superhydrophobic state was lost after 1 min (48 cycles), resulting in the WCA of $140\text{--}145^\circ$. According to our knowledge, there is no work reporting the SAR testing of hydrophobic/superhydrophobic surfaces. Nevertheless, the sand erosion test on Yb_2O_3 solution precursor atmospheric/vacuum plasma sprayed (SPAPS/SPVPS) coatings reported in (Ref 31) revealed the changes of the WCA from 163° to 96° for SPAPS and from 155° to 140° for SPVPS after 25 s of testing, which provides at least some comparison. Re-covering of the samples by silicone oil turned the coatings' wetting behavior into the superhydrophobic state again, with the WCA $\sim 170^\circ$. Nevertheless, further

Fig. 13 Water contact angle of the C16 and CU16 samples after the SAR test

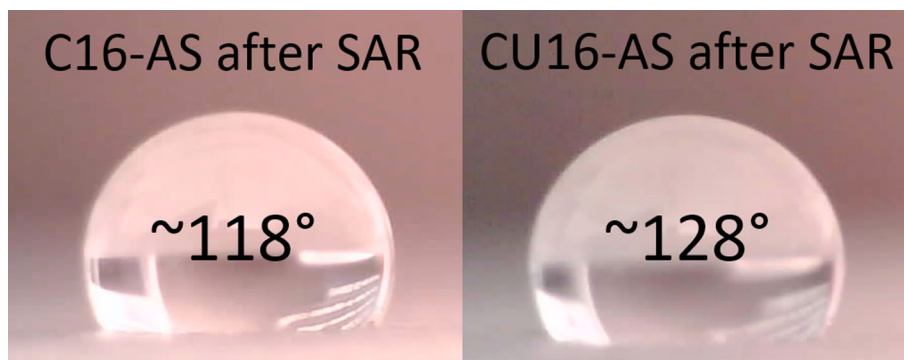


Table 8 The surface roughness parameters of C16 and CU16 samples after the SAR test

Sample	Sa, μm	Sq, μm	Ssk	Sku	Rs
C16 AS	2.7 ± 0.5	3.4 ± 0.5	-0.17 ± 0.10	3.19 ± 0.10	1.39 ± 0.05
CU16 AS	3.6 ± 0.3	4.4 ± 0.4	-0.28 ± 0.10	2.82 ± 0.20	1.48 ± 0.03

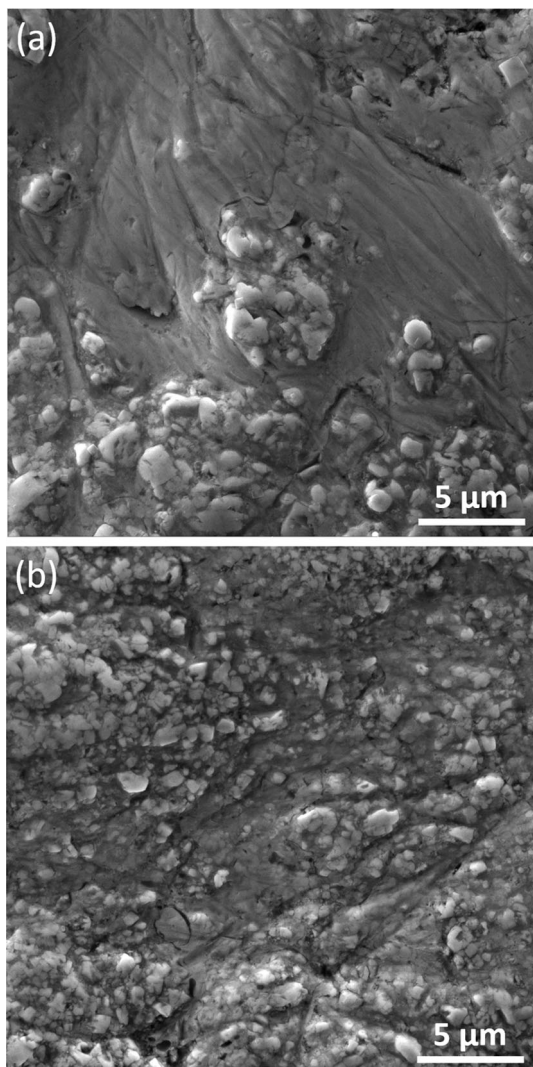


Fig. 14 Top-view of C16 (a) and CU16 (b) coatings after the SAR test

research on surface modifications with higher mechanical stability is clearly needed.

Conclusions

The investigation of water wetting behavior of high velocity oxy-fuel hard cermet WC-Co-Cr coatings produced from three different feedstock powders was carried out. To understand the impact of different feedstock powders (C16—coarse with coarse WC particles, CU16—coarse with ultrafine WC particles and CU31—fine with ultrafine WC particles) on surface chemistry and surface topography and their further influence on the wetting behavior, the experimental coatings were studied in four states (as-sprayed, polished, as-sprayed modified and polished modified).

All the samples showed the hydrophilic behavior in the polished state, whereas in the as-sprayed state, all samples were hydrophobic. Higher hydrophobicity of C16 and CU16 as-sprayed samples was related to higher surface roughness factor that was promoted by spraying coarser powders. This is the first study reporting WC-Co-Cr cermet coatings with water contact angle as high as 143° in the as-sprayed state. Such wetting behavior relates to a unique combination of chemical composition and multi-scale surface topography enabled by fine WC carbide particles in the feedstock powder. The additional surface chemistry modification with the Si oil layer turned the coatings into the superhydrophobic state with the lotus effect, resulting in the water contact angle above 150° and the sliding angle below 10° . The highest hydrophobicity in the as-sprayed (WCA $\sim 143^\circ$) and as-sprayed modified (WCA $> 170^\circ$ and sliding angle $\sim 5^\circ$) states was found for the CU16 coating produced from coarse powder with ultrafine WC

particles, which yielded nano-scale topographical features on the surface of micron-sized splats and the highest surface roughness factor R_s . This was associated with the Cassie–Baxter wetting regime with air pockets trapped between the liquid and solid surfaces, providing high water repellency and water mobility. The combined Cassie–Baxter/Wenzel equation was used to estimate that in this case only 3.8% of water droplet area was related to the solid–liquid contact, while 96.2% of area was occupied by the air–liquid interface. Therefore, it can be concluded that the combination of a coarse powder with ultrafine WC particles can be used to produce highly hydrophobic hard as-sprayed coatings, which can be further turned superhydrophobic by additional surface chemistry modification.

The preliminary results of the slurry abrasion response test showed very good robustness of hydrophobicity of the C16 and CU16 coatings. The presence of the wear tracks and WC particles on the surfaces resulted in the WCA of 118° (C16) and 128° (CU16) after 11 520 cycles, proving that the hydrophobicity can be sustained during the lifetime even in some sacrificial applications. However, the superhydrophobic state of the modified coatings was lost after 48 cycles pointing to the need for further research on mechanically stable surface modifications.

Acknowledgment This research was made in the frame of the Specific Research Project CEITEC VUT-J-19-5799 awarded at the Central European Institute of Technology – Brno University of Technology. We acknowledge CzechNanoLab Research Infrastructure supported by MEYS CR (LM2018110). The help of Ing. Subhash Gupta within the XPS analysis is thankfully acknowledged.

References

1. Y. Yuan and T.R. Lee, Contact Angle and Wetting Properties, *Surface Science Techniques Springer Series in Surface Sciences*, Vol 51, G. Bracco and B. Holst, Ed., Springer, Berlin, 2013,
2. A. Lafuma and D. Quéré, Superhydrophobic States, *Nat. Mater.*, 2003, **2**, p 457–460. <https://doi.org/10.1038/nmat924>
3. J. Drelich and E. Chibowski, Superhydrophilic and Superwetting Surfaces: Definition and Mechanisms of Control, *Langmuir*, 2010, **26**(24), p 18621–18623. <https://doi.org/10.1021/la1039893>
4. T. Young, An Essay to the Cohesion of Fluids, *Philosophical Trans. R. Soc. London.*, 1804, **95**, p 65–87. <https://doi.org/10.1098/rstb.1983.0080>
5. R.N. Wenzel, Resistance of Solid Surfaces to Wetting by Water, *Ind. Eng. Chem.*, 1936, **28**(8), p 988–994. <https://doi.org/10.1021/ie50320a024>
6. B.D. Cassie, A.B.D. Cassie, and S. Baxter, Of Porous Surfaces, *Trans. Faraday Soc.*, 1944, **40**, p 546–551. <https://doi.org/10.1039/tf9444000546>
7. T. Nishino, M. Meguro, K. Nakamae, M. Matsushita, and Y. Ueda, The Lowest Surface free Energy Based on -CF₃ Alignment, *Langmuir*, 1999, **15**(13), p 4321–4323. <https://doi.org/10.1021/la981727s>
8. Y.Y. Yan, N. Gao, and W. Barthlott, Mimicking Natural Superhydrophobic Surfaces and Grasping the Wetting Process: A Review on Recent Progress in Preparing Superhydrophobic Surfaces, *Adv. Colloid Interface Sci.*, 2011, **169**(2), p 80–105. <https://doi.org/10.1016/j.cis.2011.08.005>
9. L.B. Boinovich and A.M. Emelyanenko, Hydrophobic Materials and Coatings: Principles of Design, Properties and Applications, *Russ. Chem. Rev.*, 2008, **77**(7), p 583–600. <https://doi.org/10.1070/RC2008v077n07ABEH003775>
10. J. Drelich, E. Chibowski, D.D. Meng, and K. Terpilowski, Hydrophilic and Superhydrophilic Surfaces and Materials, *Soft Matter*, 2011, **7**, p 9804–9828. <https://doi.org/10.1039/c1sm05849e>
11. J. Genzer and K. Efimenko, Recent Developments in Superhydrophobic Surfaces and Their Relevance to Marine Fouling: A Review, *Biofouling*, 2006, **22**(5), p 339–360. <https://doi.org/10.1080/08927010600980223>
12. K. Liu and L. Jiang, Bio-Inspired Self-Cleaning Surfaces, *Annu. Rev. Mater. Res.*, 2012, **42**(1), p 231–263. <https://doi.org/10.1146/annurev-matsci-070511-155046>
13. R. Blossey, Self-Cleaning Surfaces—Virtual Realities, *Nat. Mater.*, 2003, **2**, p 301–306. <https://doi.org/10.1038/nmat856>
14. M. Zhang, C. Wang, S. Wang, and J. Li, Fabrication of Superhydrophobic Cotton Textiles for Water–Oil Separation Based on Drop-Coating Route, *Carbohydr. Polym.*, 2013, **97**(1), p 59–64. <https://doi.org/10.1016/j.carbpol.2012.08.118>
15. J.B. Boreyko and C.-H. Chen, Self-Propelled Dropwise Condensate on Superhydrophobic Surfaces, *Phys. Rev. Lett.*, 2009, **103**(18), p 184501. <https://doi.org/10.1103/PhysRevLett.103.184501>
16. K.M. Wisdom, J.A. Watson, X. Qu, F. Liu, G.S. Watson, and C.-H. Chen, Self-Cleaning of Superhydrophobic Surfaces by Self-Propelled Jumping Condensate, *Proc. Natl. Acad. Sci.*, 2013, **110**(20), p 7992–7997. <https://doi.org/10.1073/pnas.1210770110>
17. H. Koivuluoto, E. Hartikainen, and H. Niemela-Anttonen, Thermally Sprayed Coatings: Novel Surface Engineering Strategy Towards Icephobic Solutions, *Materials*, 2020, **13**(6), p 1434. <https://doi.org/10.3390/ma13061434>
18. H. Sojoudi, M. Wang, N.D. Boscher, G.H. McKinley, and K.K. Gleason, Durable and Scalable Icephobic Surfaces: Similarities and Distinctions From Superhydrophobic Surfaces, *Soft Matter*, 2016, **12**, p 1938–1963. <https://doi.org/10.1039/C5SM02295A>
19. Q. Xu, J. Li, J. Tian, J. Zhu, and X. Gao, Energy-Effective Frost-Free Coatings Based on Superhydrophobic Aligned Nanocones, *ACS Appl. Mater. Interfaces.*, 2014, **6**(12), p 8976–8980. <https://doi.org/10.1021/am502607e>
20. T. Moriya, K. Manabe, M. Tenjimbayashi, K. Suwabe, H. Tsuchiya, T. Matsubayashi, W. Navarrini, and S. Shiratori, A Superrepellent Coating with Dynamic Fluorine Chains for Frosting Suppression: Effects of Polarity, Coalescence and Ice Nucleation Free Energy Barrier, *RSC Adv.*, 2016, **6**, p 92197–92205. <https://doi.org/10.1039/C6RA18483A>
21. Gh Barati Darband, M. Aliofjhzraei, S. Khorsand, S. Sokhanvar, and A. Kaboli, Science and Engineering of Superhydrophobic Surfaces: Review of Corrosion Resistance, Chemical and Mechanical Stability, *Arab. J. Chem.*, 2020, **13**(1), p 1763–1802. <https://doi.org/10.1016/j.arabjc.2018.01.013>
22. C. Lee and C.-J. Kim, Underwater Restoration and Retention of Gases on Superhydrophobic Surfaces for Drag Reduction, *Phys. Rev. Lett.*, 2011, **106**(1), p 014502. <https://doi.org/10.1103/PhysRevLett.106.014502>
23. A.M. Emelyanenko, F.M. Shagieva, A.G. Domantovsky, and L.B. Boinovich, Nanosecond laser Micro- and Nanotexturing for the Design of a Superhydrophobic Coating Robust Against Long-Term Contact With Water, Cavitation, and Abrasion, *Appl. Surf. Sci.*, 2015, **332**, p 513–517. <https://doi.org/10.1016/j.apsusc.2015.01.202>
24. Y. Tian and L. Jiang, Intrinsically Robust Hydrophobicity, *Nat. Mater.*, 2013, **12**, p 291–292. <https://doi.org/10.1038/nmat3610>

25. P. Komarov, L. Čelko, M. Remešová, K. Skorokhod, D. Jech, L. Klakurková, K. Slámečka and R. Mušálek, The role of microstructure on wettability of plasma sprayed yttria stabilized zirconia coatings, in: *Met. 2017 - 26th Int. Conf. Metall. Mater.*, TANGER Ltd, 2017: pp. 1116–1121.
26. K. Koch, B. Bhushan, Y.C. Jung, and W. Barthlott, Fabrication of Artificial Lotus Leaves and Significance of Hierarchical Structure For Superhydrophobicity and Low Adhesion, *Soft Matter*, 2009, **5**, p 1386. <https://doi.org/10.1039/b818940d>
27. T. Verho, C. Bower, P. Andrew, S. Franssila, O. Ikkala, and R.H.A. Ras, Mechanically Durable Superhydrophobic Surfaces, *Adv. Mater.*, 2011, **23**(5), p 673-678. <https://doi.org/10.1002/adma.201003129>
28. N. Sharifi, M. Pugh, C. Moreau, and A. Dolatabadi, Developing Hydrophobic and Superhydrophobic TiO₂ Coatings by Plasma Spraying, *Surf. Coat. Technol.*, 2016, **289**, p 29-36. <https://doi.org/10.1016/j.surfcoat.2016.01.029>
29. L. Hu, X. Song, D. Jin, C. Xing, X. Shan, X. Zhao, F. Guo, and P. Xiao, A Robust Quasi-Superhydrophobic Ceria Coating Prepared Using Air-Plasma Spraying, *J. Am. Ceram. Soc.*, 2019, **102**(3), p 1386-1393. <https://doi.org/10.1111/jace.16005>
30. P. Xu, T.W. Coyle, L. Pershin, and J. Mostaghimi, Fabrication of Micro-/Nano-Structured Superhydrophobic Ceramic Coating with Reversible Wettability Via A Novel Solution Precursor Vacuum Plasma Spray Process, *Mater. Des.*, 2018, **160**, p 974-984. <https://doi.org/10.1016/j.matdes.2018.10.015>
31. P. Xu, T.W. Coyle, L. Pershin, and J. Mostaghimi, Understanding the Correlations Between the Mechanical Robustness, Coating Structures and Surface Composition for Highly-/Super-Hydrophobic Ceramic Coatings, *Surf. Coat. Technol.*, 2019, **378**, p 124929. <https://doi.org/10.1016/j.surfcoat.2019.124929>
32. N. Xi, Y. Liu, X. Zhang, N. Liu, H. Fu, Z. Hang, G. Yang, H. Chen, and W. Gao, Steady Anti-Icing Coatings on Weathering Steel Fabricated by HVOF Spraying, *Appl. Surf. Sci.*, 2018, **444**, p 757-762. <https://doi.org/10.1016/j.apsusc.2018.03.075>
33. J. Qiao, L. Na Zhu, W. Yue, Z. Qiang Fu, J. Jie Kang, and C. Biao Wang, The Effect of Attributes of Micro-Shapes of Laser Surface Texture on the Wettability of WC-CrCo Metal Ceramic Coatings, *Surf. Coat. Technol.*, 2018, **334**, p 429-437. <https://doi.org/10.1016/j.surfcoat.2017.12.001>
34. S. Vijay, L. Wang, C. Lyphout, P. Nylen, and N. Markocsan, Surface Characteristics Investigation of HVOF Sprayed Cermet Coatings, *Appl. Surf. Sci.*, 2019, **493**, p 956-962. <https://doi.org/10.1016/j.apsusc.2019.07.079>
35. P. Komarov, L. Čelko, D. Jech, M. Papula, K. Slámečka, M. Horynová, L. Klakurková, and J. Kaiser, Investigations of Wettability of Wear Resistant Coatings Produced by Atmospheric Plasma Spraying, *Solid State Phenom.*, 2017, **270**, p 230-235. <https://doi.org/10.4028/www.scientific.net/SSP.270.230>
36. J. Pulsford, S. Kamnis, J. Murray, M. Bai, and T. Hussain, Effect of Particle and Carbide Grain Sizes on a HVOAF WC-Co-Cr Coating for the Future Application on Internal Surfaces: Microstructure and Wear, *J. Therm. Spray Technol.*, 2018, **27**, p 207-219. <https://doi.org/10.1007/s11666-017-0669-8>
37. H. Wang, M. Gee, Q. Qiu, H. Zhang, X. Liu, H. Nie, X. Song, and Z. Nie, Grain size Effect on Wear Resistance of WC-Co Cemented Carbides Under Different Tribological Conditions, *J. Mat. Sci. Tech.*, 2019, **35**, p 2435-2446. <https://doi.org/10.1016/j.jmst.2019.07.016>
38. J.M. Guilemany, S. Dosta, and J.R. Miguel, The Enhancement of the Properties of WC-Co HVOF Coatings Through the Use of Nanostructured and Microstructured Feedstock Powders, *Surf. Coat. Technol.*, 2006, **201**(3-4), p 1180-1190. <https://doi.org/10.1016/j.surfcoat.2006.01.041>
39. A. Lekatou, D. Sioulas, A.E. Karantzalis, and D. Grimanelis, A Comparative Study on the Microstructure and Surface Property Evaluation of Coatings Produced from Nanostructured and Conventional WC-Co Powders HVOF-Sprayed on Al7075, *Surf. Coat. Technol.*, 2015, **276**, p 539-556. <https://doi.org/10.1016/j.surfcoat.2015.06.017>
40. B. Yin, H.D. Zhou, D.L. Yi, J.M. Chen, and F.Y. Yan, Microsliding Wear Behaviour of HVOF Sprayed Conventional and Nanostructured WC-12Co Coatings at Elevated Temperatures, *Surf. Eng.*, 2013, **26**(6), p 469-477. <https://doi.org/10.1179/026708410X12506870724352>
41. A. Larson, R. Dreele, General Structure Analysis System (GSAS). LAUR 86-748. <https://doi.org/10.https://11bm.xray.aps.anl.gov/documents/GSASManual.pdf>, 2004 (accessed 31 July 2020).
42. J.A.R. Wesmann and N. Espallargas, Elucidating the Complex Role of Surface Oxides Formed During Sliding of selfMated Warm Sprayed WC-CoCr in Different Environments, *Trib. Int.*, 2016, **94**, p 360-372. <https://doi.org/10.1016/j.triboint.2015.09.043>
43. J.A.R. Wesmann, S. Kuroda, and N. Espallargas, The Role of Oxide Tribofilms on Friction and Wear of Different Thermally Sprayed WC-CoCr, *J. Therm. Spray Technol.*, 2017, **26**, p 492-502. <https://doi.org/10.1007/s11666-017-0522-0>
44. L.-N. Zhang, Y.-Y. Ma, Z.-L. Lang, Y.-H. Wang, S.U. Khan, G. Yan, H.-Q. Tan, H.-Y. Zang, and Y.-G. Li, Ultrafine Cable-Like WC/W₂C Heterojunction Nanowires Covered by Graphitic Carbon Towards Highly Efficient Electrocatalytic Hydrogen Evolution, *J. Mater. Chem. A*, 2018, **6**, p 15395-15403. <https://doi.org/10.1039/C8TA05007D>
45. J.A. Picas, M. Punset, E. Ruperez, S. Menargues, E. Martin, and M.T. Baile, Corrosion Mechanism of HVOF Thermal Sprayed WC-CoCr Coatings in Acidic Chloride Media, *Surf. Coat. Technol.*, 2019, **371**, p 378-388. <https://doi.org/10.1016/j.surfcoat.2018.10.025>
46. Z. Chen, W. Gong, S. Cong, Z. Wang, G. Song, T. Pan, X. Tang, J. Chen, W. Lu, and Z. Zhao, Eutectoid-Structured WC/W₂C Heterostructures: A New Platform for Long-Term Alkaline Hydrogen Evolution Reaction at Low Overpotentials, *Nano Energy*, 2020, **68**, p 104335. <https://doi.org/10.1016/j.nanoen.2019.104335>
47. ISO 25178 part 2, Geometrical Product Specification (GPS) - Surface Texture: Areal - Part 2: Terms, Definitions and Surface Texture Parameters, International Organization for Standardization, 2012.
48. K. Slámečka, D. Jech, L. Klakurková, S. Tkachenko, M. Remešová, P. Gejdoš, and L. Čelko, Thermal Cycling Damage in Pre-Oxidized Plasma-Sprayed MCrAlY + YSZ Thermal Barrier Coatings: Phenomenon Of Multiple Parallel Delamination of the TGO Layer, *Surf. Coat. Technol.*, 2020, **384**, p 125328. <https://doi.org/10.1016/j.surfcoat.2019.125328>
49. D.K. Owens and R.C. Wendt, Estimation of the Surface Free Energy of Polymers, *J. Appl. Polym. Sci.*, 1969, **13**(8), p 1741-1747. <https://doi.org/10.1002/app.1969.070130815>
50. J.M. Schuster, C.E. Schvezov, and M.R. Rosenberger, Analysis of the Results of Surface Free Energy Measurement of Ti6Al4V by Different Methods, *Procedia Mater. Sci.*, 2015, **8**, p 732-741. <https://doi.org/10.1016/j.mspro.2015.04.130>
51. G75-15 Standard Test Method for Determination of Slurry Abrasivity (Miller Number) and Slurry Abrasion Response of Materials (SAR Number), ASTM International, 2015. <https://doi.org/10.1520/G0075-15>
52. S. Al-Mutairi, M.S.J. Hashmi, B.S. Yilbas, and J. Stokes, Microstructural Characterization of HVOF/plasma Thermal Spray of Micro/Nano WC-12%Co powders, *Surf. Coat. Technol.*, 2015, **264**, p 175-186. <https://doi.org/10.1016/j.surfcoat.2014.12.050>

53. Q. Yang, T. Senda, and A. Ohmori, Effect of Carbide Grain Size on Microstructure and Sliding Wear Behavior of HVOF-Sprayed WC–12% Co Coatings, *Wear*, 2003, **254**(1–2), p 23–34. [https://doi.org/10.1016/S0043-1648\(02\)00294-6](https://doi.org/10.1016/S0043-1648(02)00294-6)
54. M. Li and P.D. Christofides, Computational Study of Particle in-Flight Behavior in the HVOF Thermal Spray Process, *Chem. Eng. Sci.*, 2006, **61**(19), p 6540–6552. <https://doi.org/10.1016/j.ces.2006.05.050>
55. C.J. Li, A. Ohmori, and Y. Harada, Formation of an Amorphous Phase in Thermally Sprayed WC-Co, *J. Therm. Spray Technol.*, 1996, **5**, p 69–73. <https://doi.org/10.1007/BF02647520>
56. M. Federici, C. Menapace, A. Moscatelli, S. Gialanella, and G. Straffelini, Pin-on-Disc Study of a Friction Material Dry Sliding Against HVOF Coated Discs at Room Temperature and 300°C, *Tribol. Int.*, 2017, **115**, p 89–99. <https://doi.org/10.1016/j.triboint.2017.05.030>
57. S.M. Nahvi and M. Jafari, Microstructural and Mechanical Properties of Advanced HVOF-Sprayed WC-Based Cermet Coatings, *Surf. Coat. Technol.*, 2016, **286**, p 95–102. <https://doi.org/10.1016/j.surfcoat.2015.12.016>
58. X. Ding, X.D. Cheng, C. Li, X. Yu, Z.X. Ding, and C.Q. Yuan, Microstructure and Performance of Multi-Dimensional WC-CoCr Coating Sprayed by HVOF, *Int. J. Adv. Manuf. Technol.*, 2018, **96**, p 1625–1633. <https://doi.org/10.1007/s00170-017-0837-5>
59. R. Vaßen, G. Kerhoff, D. Stöver, Development of a micromechanical life prediction model for plasma sprayed thermal barrier coatings, *Mat. Sci. and Eng.:A*, **303** (1–2), p 100–109. [https://doi.org/10.1016/S0921-5093\(00\)01853-0](https://doi.org/10.1016/S0921-5093(00)01853-0)
60. W. Tillmann, L. Hagen, D. Stangier, M. Krabiell, P. Schröder, J. Tiller, C. Krumm, C. Sternemann, M. Paulus, and M. Elbers, Influence of Etching-Pretreatment on Nano-Grained WC-Co Surfaces and Properties of PVD/HVOF Duplex Coatings, *Surf. Coat. Technol.*, 2019, **374**, p 32–43. <https://doi.org/10.1016/j.surfcoat.2019.05.054>
61. P. Xu, G. Meng, L. Pershin, J. Mostaghimi, and T.W. Coyle, Control of the Hydrophobicity of Rare Earth Oxide Coatings Deposited by Solution Precursor Plasma Spray by Hydrocarbon Adsorption, *J. Mat. Sci. Tech.*, 2021, **62**, p 107–118. <https://doi.org/10.1016/j.jmst.2020.04.044>
62. J. Li, C. Li, G. Yan, and C. Li, Wettability Transition on Micro-Nano Hierarchical Structured Ni20Cr Coating Surface by Selective Spontaneous Adsorption During Vacuum Evacuation, *Mater. Chem. Phys.*, 2018, **219**, p 292–302. <https://doi.org/10.1016/j.matchemphys.2018.08.049>
63. M. Morra, E. Occhiello, R. Marola, F. Garbassi, P. Humphrey, and D. Johnson, On the Aging of Oxygen Plasma-Treated Polydimethylsiloxane Surfaces, *J. Colloid Interface Sci.*, 1990, **137**(1), p 11–24. [https://doi.org/10.1016/0021-9797\(90\)90038-P](https://doi.org/10.1016/0021-9797(90)90038-P)

Publisher's Note Springer Nature remains neutral with regard to jurisdictional claims in published maps and institutional affiliations.